Active Damping of Rotating Positioning Platforms using Force Feedback

T. Dehaeze [1,3], **C. Collette** [1,2]
[1] Precision Mechatronics Laboratory
University of Liege, Belgium

[2] BEAMS Department
Free University of Brussels, Belgium

[3] European Synchrotron Radiation Facility
Grenoble, France e-mail: **thomas.dehaeze@esrf.fr**

Abstract
Abstract text to be done

1 Introduction

Due to gyroscopic effects, the guaranteed robustness properties of Integral Force Feedback do not hold. Either the control architecture can be slightly modified or mechanical changes in the system can be performed. This paper has been published The Matlab code that was use to obtain the results are available in [1].

2 Dynamics of Rotating Positioning Platforms

2.1 Model of a Rotating Positioning Platform

In order to study how the rotation of a positioning platforms does affect the use of integral force feedback, a model of an XY positioning stage on top of a rotating stage is developed.

The model is schematically represented in Figure 1 and forms the simplest system where gyroscopic forces can be studied.

The rotating stage is supposed to be ideal, meaning it induces a perfect rotation $\theta(t) = \Omega t$ where Ω is the rotational speed in $\mathrm{rad\,s^{-1}}$.

The parallel XY positioning stage consists of two orthogonal actuators represented by three elements in parallel: a spring with a stiffness k in $\mathrm{N\,m^{-1}}$, a dashpot with a damping coefficient c in $\mathrm{N\,m^{-1}\,s}$ and an ideal force source F_u, F_v. A payload with a mass m in kg is mounted on the (rotating) XY stage.

Two reference frames are used: an inertial frame $(\vec{i}_x, \vec{i}_y, \vec{i}_z)$ and a uniform rotating frame $(\vec{i}_u, \vec{i}_v, \vec{i}_w)$ rigidly fixed on top of the rotating stage with $\vec{i}_w$ aligned with the rotation axis. The position of the payload is represented by $(d_u, d_v, 0)$ expressed in the rotating frame.

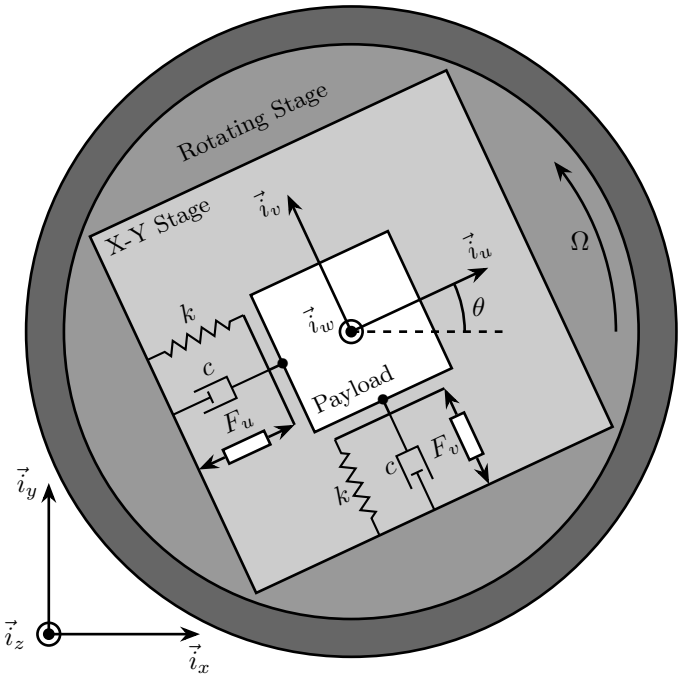

Figure 1: Schematic of the studied System

2.2 Equations of Motion

To obtain of equation of motion for the system represented in Figure 1, the Lagrangian equations are used:

$$\frac{d}{dt}\left(\frac{\partial L}{\partial \dot{q}_i}\right) + \frac{\partial D}{\partial \dot{q}_i} - \frac{\partial L}{\partial q_i} = Q_i \tag{1}$$

with $L = T - V$ the Lagrangian, D the dissipation function, and Q_i the generalized force associated with the generalized variable $\begin{bmatrix} q_1 & q_2 \end{bmatrix} = \begin{bmatrix} d_u & d_v \end{bmatrix}$.

The constant rotation in the $(\vec{i}_x, \vec{i}_y)$ plane is here disregarded as it is imposed by the ideal rotating stage.

$$T = \frac{1}{2} m \left(\left(\dot{d}_u - \Omega d_v \right)^2 + \left(\dot{d}_v + \Omega d_u \right)^2 \right) \tag{2a}$$

$$V = \frac{1}{2} k \left({d_u}^2 + {d_v}^2 \right) \tag{2b}$$

$$D = \frac{1}{2} c \left({\dot{d}_u}^2 + {\dot{d}_v}^2 \right) \tag{2c}$$

$$Q_1 = F_u, \quad Q_2 = F_v \tag{2d}$$

Substituting equations (2) into (1) gives two coupled differential equations

$$m\ddot{d}_u + c\dot{d}_u + (k - m\Omega^2) d_u = F_u + 2m\Omega\dot{d}_v \tag{3a}$$

$$m\ddot{d}_v + c\dot{d}_v + (k \underbrace{- m\Omega^2}_{\text{Centrif.}}) d_v = F_v \underbrace{- 2m\Omega\dot{d}_u}_{\text{Coriolis}} \tag{3b}$$

The uniform rotation of the system induces two Gyroscopic effects as shown in Eq. (3):

- Centrifugal forces: that can been seen as added negative stiffness $-m\Omega^2$ along $\vec{i}_u$ and $\vec{i}_v$
- Coriolis Forces: that couples the motion in the two orthogonal directions

One can verify that without rotation ($\Omega = 0$) the system becomes equivalent as to two uncoupled one degree

of freedom mass-spring-damper systems:

$$m\ddot{d}_u + c\dot{d}_u + kd_u = F_u \tag{4a}$$
$$m\ddot{d}_v + c\dot{d}_v + kd_v = F_v \tag{4b}$$

2.3 Transfer Functions in the Laplace domain

To study the dynamics of the system, the differential equations of motions (3) are transformed in the Laplace domain and the 2×2 transfer function matrix $\boldsymbol{G}_d$ from $\begin{bmatrix} F_u & F_v \end{bmatrix}$ to $\begin{bmatrix} d_u & d_v \end{bmatrix}$ is obtained

$$\begin{bmatrix} d_u \\ d_v \end{bmatrix} = \boldsymbol{G}_d \begin{bmatrix} F_u \\ F_v \end{bmatrix} \tag{5}$$

$$\boldsymbol{G}_d = \begin{bmatrix} \frac{ms^2+cs+k-m\Omega^2}{(ms^2+cs+k-m\Omega^2)^2+(2m\Omega s)^2} & \frac{2m\Omega s}{(ms^2+cs+k-m\Omega^2)^2+(2m\Omega s)^2} \\ \frac{-2m\Omega s}{(ms^2+cs+k-m\Omega^2)^2+(2m\Omega s)^2} & \frac{ms^2+cs+k-m\Omega^2}{(ms^2+cs+k-m\Omega^2)^2+(2m\Omega s)^2} \end{bmatrix} \tag{6}$$

To simplify the analysis, the undamped natural frequency ω_0 and the damping ratio ξ are used

$$\omega_0 = \sqrt{\frac{k}{m}} \text{ in } \mathrm{rad\,s^{-1}} \tag{7a}$$
$$\xi = \frac{c}{2\sqrt{km}} \tag{7b}$$

The transfer function matrix $\boldsymbol{G}_d$ (6) becomes equal to

$$\boldsymbol{G}_d = \frac{1}{k} \begin{bmatrix} \frac{\frac{s^2}{{\omega_0}^2}+2\xi\frac{s}{\omega_0}+1-\frac{\Omega^2}{{\omega_0}^2}}{\left(\frac{s^2}{{\omega_0}^2}+2\xi\frac{s}{\omega_0}+1-\frac{\Omega^2}{{\omega_0}^2}\right)^2+\left(2\frac{\Omega}{\omega_0}\frac{s}{\omega_0}\right)^2} & \frac{2\frac{\Omega}{\omega_0}\frac{s}{\omega_0}}{\left(\frac{s^2}{{\omega_0}^2}+2\xi\frac{s}{\omega_0}+1-\frac{\Omega^2}{{\omega_0}^2}\right)^2+\left(2\frac{\Omega}{\omega_0}\frac{s}{\omega_0}\right)^2} \\ \frac{-2\frac{\Omega}{\omega_0}\frac{s}{\omega_0}}{\left(\frac{s^2}{{\omega_0}^2}+2\xi\frac{s}{\omega_0}+1-\frac{\Omega^2}{{\omega_0}^2}\right)^2+\left(2\frac{\Omega}{\omega_0}\frac{s}{\omega_0}\right)^2} & \frac{\frac{s^2}{{\omega_0}^2}+2\xi\frac{s}{\omega_0}+1-\frac{\Omega^2}{{\omega_0}^2}}{\left(\frac{s^2}{{\omega_0}^2}+2\xi\frac{s}{\omega_0}+1-\frac{\Omega^2}{{\omega_0}^2}\right)^2+\left(2\frac{\Omega}{\omega_0}\frac{s}{\omega_0}\right)^2} \end{bmatrix} \tag{8}$$

For all the numerical analysis in this study, $\omega_0 = 1\,\mathrm{rad\,s^{-1}}$, $k = 1\,\mathrm{N\,m^{-1}}$ and $\xi = 0.025 = 2.5\,\%$.

Even tough no system with such parameters will be encountered in practice, conclusions will be drawn relative to these parameters such that they can be generalized to any other parameter.

2.4 System Dynamics and Campbell Diagram

The poles of $\boldsymbol{G}_d$ are the complex solutions p of

$$\left(\frac{p^2}{{\omega_0}^2} + 2\xi\frac{p}{\omega_0} + 1 - \frac{\Omega^2}{{\omega_0}^2}\right)^2 + \left(2\frac{\Omega}{\omega_0}\frac{p}{\omega_0}\right)^2 = 0 \tag{9}$$

Supposing small damping ($\xi \ll 1$), two pairs of complex conjugate poles are obtained:

$$p_+ = -\xi\omega_0\left(1 + \frac{\Omega}{\omega_0}\right) \pm j\omega_0\left(1 + \frac{\Omega}{\omega_0}\right) \tag{10a}$$
$$p_- = -\xi\omega_0\left(1 - \frac{\Omega}{\omega_0}\right) \pm j\omega_0\left(1 - \frac{\Omega}{\omega_0}\right) \tag{10b}$$

The real part and complex part of these two pairs of complex conjugate poles are represented in Figure 2 as a function of the rotational speed Ω. As the rotational speed increases, p_+ goes to higher frequencies and p_-

to lower frequencies. The system becomes unstable for $\Omega > \omega_0$ as the real part of p_- is positive. Physically, the negative stiffness term $-m\Omega^2$ induced by centrifugal forces exceeds the spring stiffness k.

In the rest of this study, rotational speeds smaller than the undamped natural frequency of the system are assumed ($\Omega < \omega_0$).

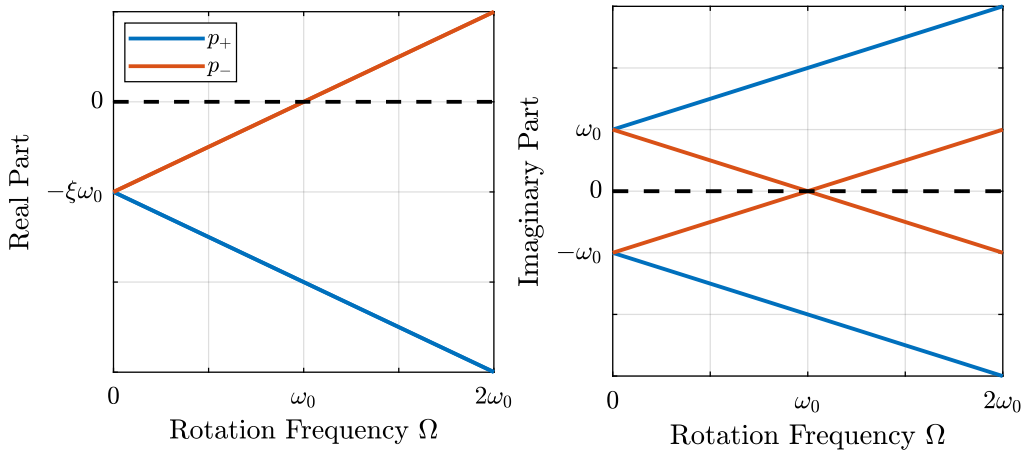

(a) Real Part (b) Imaginary Part

Figure 2: Campbell Diagram : Evolution of the complex and real parts of the system's poles as a function of the rotational speed Ω

Looking at the transfer function matrix $\boldsymbol{G}_d$ in Eq. (8), one can see that the two diagonal (direct) terms are equal and the two off-diagonal (coupling) terms are opposite. The bode plot of these two distinct terms are shown in Figure 3 for several rotational speeds Ω.

It is confirmed that the two pairs of complex conjugate poles are further separated as Ω increases. For $\Omega > \omega_0$, the low frequency complex conjugate poles p_- becomes unstable.

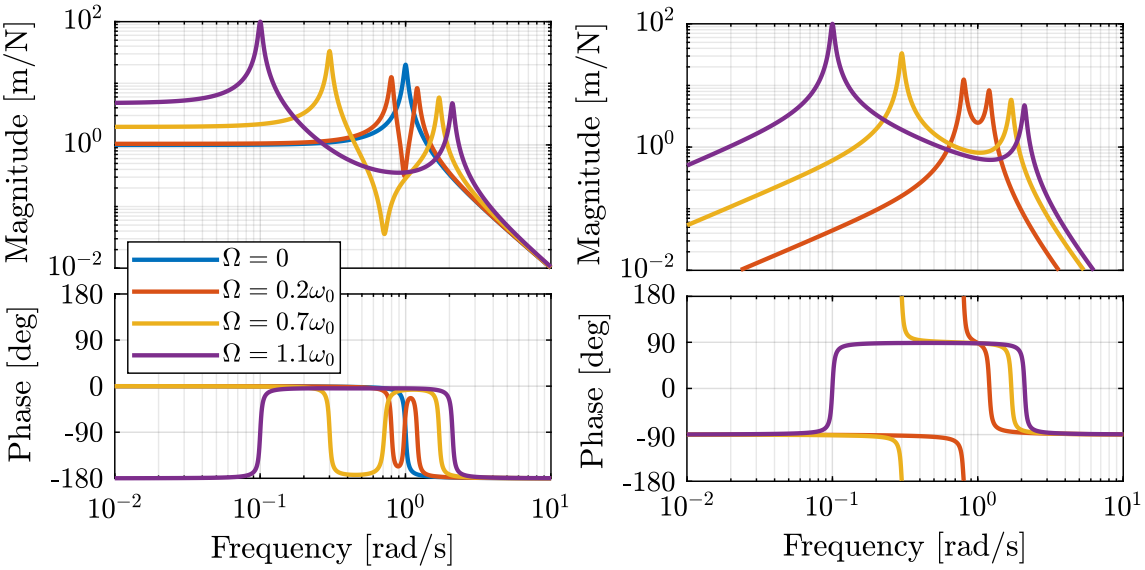

(a) Direct Terms d_u/F_u, d_v/F_v (b) Coupling Terms d_v/F_u, $-d_u/F_v$

Figure 3: Bode Plots for $\boldsymbol{G}_d$ for several rotational speed Ω

3 Decentralized Integral Force Feedback

3.1 Force Sensors and Control Architecture

In order to apply IFF to the system, force sensors are added in series with the two actuators (Figure 4). As this study focuses on decentralized control, two identical controllers K_F are used to feedback each of the sensed force to its associated actuator and no attempt is made to counteract the interactions in the system. The control diagram is schematically shown in Figure 5.

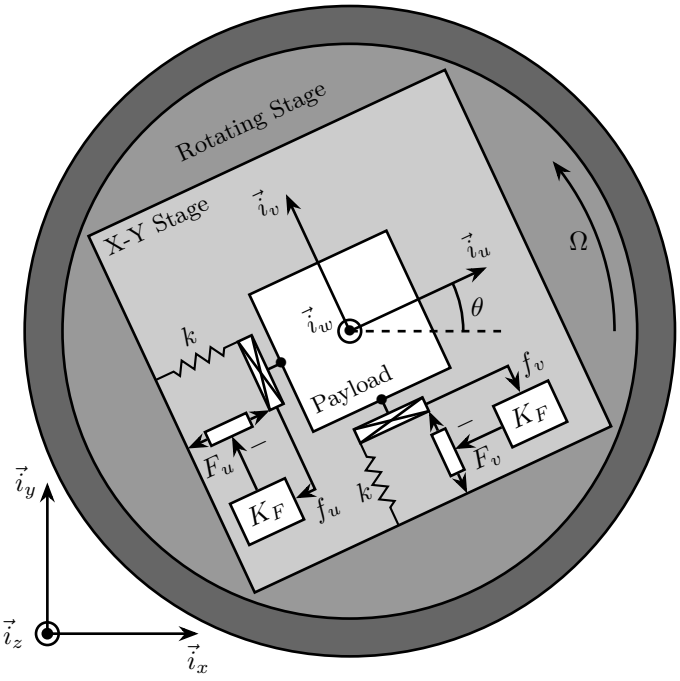

Figure 4: System with added Force Sensor in series with the actuators

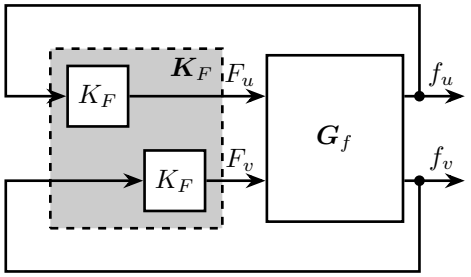

Figure 5: Control Diagram for decentralized IFF

3.2 Plant Dynamics

The forces measured by the two force sensors are equal to

$$\begin{bmatrix} f_u \\ f_v \end{bmatrix} = \begin{bmatrix} F_u \\ F_v \end{bmatrix} - (cs + k) \begin{bmatrix} d_u \\ d_v \end{bmatrix} \tag{11}$$

Re-injecting (8) into (11) yields

$$\begin{bmatrix} f_u \\ f_v \end{bmatrix} = \boldsymbol{G}_f \begin{bmatrix} F_u \\ F_v \end{bmatrix} \tag{12}$$

with $\boldsymbol{G}_f$ a 2×2 transfer function matrix

$$\boldsymbol{G}_f = \begin{bmatrix} \frac{\left(\frac{s^2}{{\omega_0}^2} - \frac{\Omega^2}{{\omega_0}^2}\right)\left(\frac{s^2}{{\omega_0}^2} + 2\xi\frac{s}{\omega_0} + 1 - \frac{\Omega^2}{{\omega_0}^2}\right) + \left(2\frac{\Omega}{\omega_0}\frac{s}{\omega_0}\right)^2}{\left(\frac{s^2}{{\omega_0}^2} + 2\xi\frac{s}{\omega_0} + 1 - \frac{\Omega^2}{{\omega_0}^2}\right)^2 + \left(2\frac{\Omega}{\omega_0}\frac{s}{\omega_0}\right)^2} & \frac{-\left(2\xi\frac{s}{\omega_0} + 1\right)\left(2\frac{\Omega}{\omega_0}\frac{s}{\omega_0}\right)}{\left(\frac{s^2}{{\omega_0}^2} + 2\xi\frac{s}{\omega_0} + 1 - \frac{\Omega^2}{{\omega_0}^2}\right)^2 + \left(2\frac{\Omega}{\omega_0}\frac{s}{\omega_0}\right)^2} \\ \frac{\left(2\xi\frac{s}{\omega_0} + 1\right)\left(2\frac{\Omega}{\omega_0}\frac{s}{\omega_0}\right)}{\left(\frac{s^2}{{\omega_0}^2} + 2\xi\frac{s}{\omega_0} + 1 - \frac{\Omega^2}{{\omega_0}^2}\right)^2 + \left(2\frac{\Omega}{\omega_0}\frac{s}{\omega_0}\right)^2} & \frac{\left(\frac{s^2}{{\omega_0}^2} - \frac{\Omega^2}{{\omega_0}^2}\right)\left(\frac{s^2}{{\omega_0}^2} + 2\xi\frac{s}{\omega_0} + 1 - \frac{\Omega^2}{{\omega_0}^2}\right) + \left(2\frac{\Omega}{\omega_0}\frac{s}{\omega_0}\right)^2}{\left(\frac{s^2}{{\omega_0}^2} + 2\xi\frac{s}{\omega_0} + 1 - \frac{\Omega^2}{{\omega_0}^2}\right)^2 + \left(2\frac{\Omega}{\omega_0}\frac{s}{\omega_0}\right)^2} \end{bmatrix} \tag{13}$$

The zeros of the diagonal terms of $\boldsymbol{G}_f$ are equal to (neglecting the damping for simplicity)

$$z_c = \pm j\omega_0 \sqrt{\frac{1}{2}\sqrt{8\frac{\Omega^2}{{\omega_0}^2}+1} + \frac{\Omega^2}{{\omega_0}^2} + \frac{1}{2}} \tag{14a}$$

$$z_r = \pm \omega_0 \sqrt{\frac{1}{2}\sqrt{8\frac{\Omega^2}{{\omega_0}^2}+1} - \frac{\Omega^2}{{\omega_0}^2} - \frac{1}{2}} \tag{14b}$$

It can be easily shown that the frequency of the two complex conjugate zeros z_c (14a) lies between the frequency of the two pairs of complex conjugate poles p_- and p_+ (10).

For non-null rotational speeds, two real zeros z_r (14b) appear in the diagonal terms inducing a non-minimum phase behavior. This can be seen in the Bode plot of the diagonal terms (Figure 6) where the magnitude experiences an increase of its slope without any change of phase.

Similarly, the low frequency gain of $\boldsymbol{G}_f$ is no longer zero and increases with the rotational speed Ω

$$\lim_{\omega \to 0} |\boldsymbol{G}_f(j\omega)| = \begin{bmatrix} \frac{\Omega^2}{{\omega_0}^2 - \Omega^2} & 0 \\ 0 & \frac{\Omega^2}{{\omega_0}^2 - \Omega^2} \end{bmatrix} \tag{15}$$

This low frequency gain can be explained as follows: a constant force F_u induces a small displacement of the mass $d_u = \frac{F_u}{k - m\Omega^2}$, which increases the centrifugal force $m\Omega^2 d_u = \frac{\Omega^2}{{\omega_0}^2 - \Omega^2} F_u$ which is then measured by the force sensors.

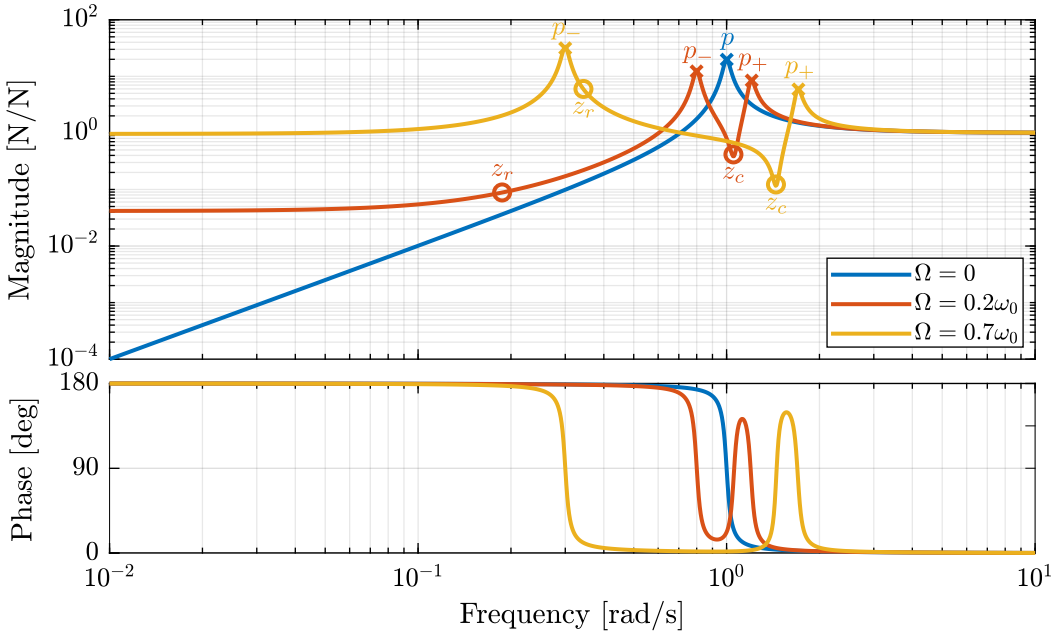

Figure 6: Bode plot of the diagonal terms of $\boldsymbol{G}_f$ for several rotational speeds Ω

3.3 Decentralized Integral Force Feedback with Pure Integrators

The two IFF controllers K_F consist of a pure integrator

$$\boldsymbol{K}_F(s) = \begin{bmatrix} K_F(s) & 0 \\ 0 & K_F(s) \end{bmatrix}, \quad K_F(s) = g \cdot \frac{1}{s} \tag{16}$$

where g is a scalar representing the gain of the controller.

In order to see how the IFF affects the poles of the closed loop system, a Root Locus (Figure 7) is constructed as follows: the poles of the closed-loop system are drawn in the complex plane as the gain g varies from 0 to ∞ for the two controllers simultaneously. As explained in [2, 3], the closed-loop poles start at the open-loop poles (shown by ✖) for $g = 0$ and coincide with the transmission zeros (shown by ○) as $g \to \infty$. The direction of increasing gain is indicated by arrows ➤.

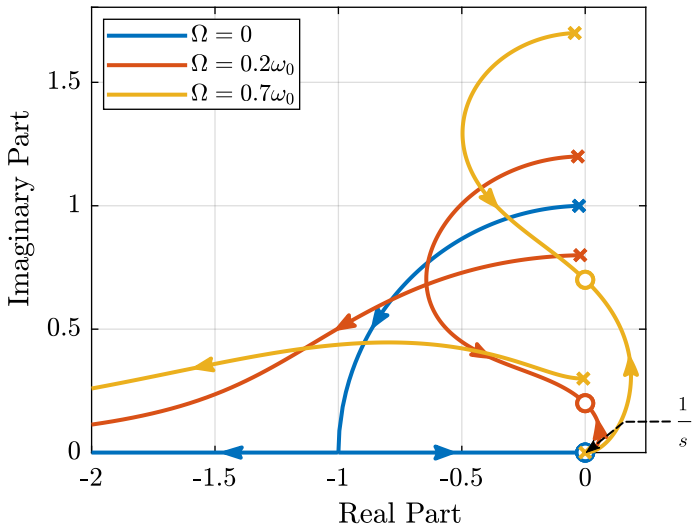

Figure 7: Root Locus for the Decentralized Integral Force Feedback for several rotating speeds Ω

Whereas collocated IFF is usually associated with unconditional stability [4], this property is lost as soon as the rotational speed in non-null due to gyroscopic effects. This can be seen in the Root Locus (Figure 7) where the pole corresponding to the controller is bounded to the right half plane implying closed-loop system instability.

Physically, this can be explained by realizing that below some frequency, the loop gain being very large, the decentralized IFF effectively decouples the payload from the XY stage. Moreover, the payload experiences centrifugal forces, which can be modeled by negative stiffnesses pulling it away from the rotation axis rendering the system unstable, hence the poles in the right half plane.

In order to apply Decentralized IFF on rotating positioning stages, two solutions are proposed to deal with this instability problem. The first one consists of slightly modifying the control law (Section 4) while the second one consists of adding springs in parallel with the force sensors (Section 5).

4 Integral Force Feedback with High Pass Filter

4.1 Modification of the Control Low

As was just explained, the instability when using IFF with pure integrators comes from the low frequency gain.

In order to limit the low frequency controller gain, an high pass filter (HPF) can be added to the controller

$$\boldsymbol{K}_F(s) = \begin{bmatrix} K_F(s) & 0 \\ 0 & K_F(s) \end{bmatrix}, \quad K_F(s) = g \cdot \frac{1}{s} \cdot \underbrace{\frac{s/\omega_i}{1 + s/\omega_i}}_{\text{HPF}} = g \cdot \frac{1}{s + \omega_i} \tag{17}$$

This is equivalent as to slightly shifting to controller pole to the left along the real axis.

This modification of the IFF controller is typically done to avoid saturation associated with the pure integrator [4]. This is however not the case in this study as it will become clear in the next section.

4.2 Feedback Analysis

The loop gains for the decentralized controllers $K_F(s)$ with and without the added HPF are shown in Figure 8. The effect of the added HPF clearly limits the low frequency gain.

The Root Loci for the decentralized IFF with and without the HPF are displayed in Figure 9. With the added HPF, the poles of the closed loop system are shown to be stable up to some value of the gain g_{max}

$$g_{\text{max}} = \omega_i \left(\frac{{\omega_0}^2}{\Omega^2} - 1 \right) \tag{18}$$

It is interesting to note that this gain g_{max} also corresponds as to when the low frequency loop gain (Figure 8) reaches one.

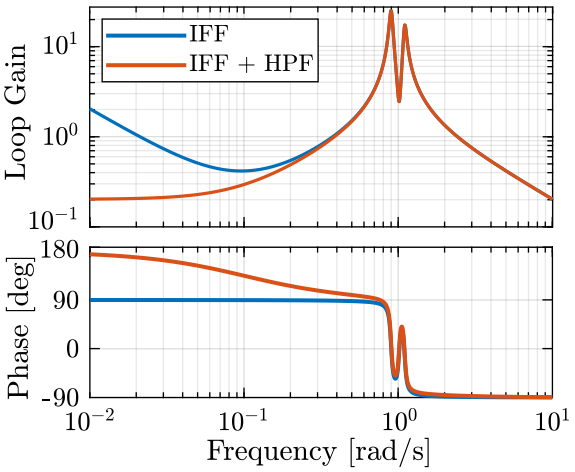

Figure 8: Modification of the loop gain with the added HFP, $g = 2$, $\omega_i = 0.1\omega_0$ and $\Omega = 0.1\omega_0$

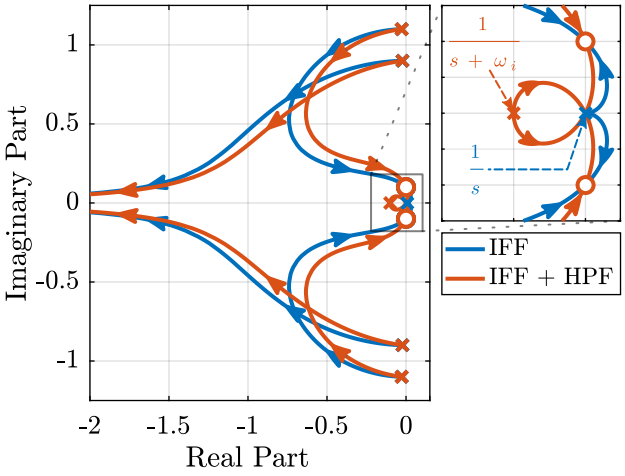

Figure 9: Modification of the Root Locus with the added HPF, $\omega_i = 0.1\omega_0$ and $\Omega = 0.1\omega_0$

4.3 Optimal Control Parameters

Two parameters can be tuned for the controller (17): the gain g and the pole's location ω_i. The optimal values of ω_i and g are here considered as the values for which the damping of all the closed-loop poles are simultaneously maximized.

In order to visualize how ω_i does affect the attainable damping, the Root Loci for several ω_i are displayed in Figure 10. It is shown that even tough small ω_i seems to allow more damping to be added to the system resonances, the control gain g may be limited to small values due to Eq. (18).

In order to study this trade off, the attainable damping ratio ξ_{cl} is computed as a function of the ratio ω_i/ω_0. The gain g_{opt} at which this maximum damping is obtained is also display and compared with the gain g_{max} at which the system becomes unstable (Figure 11)r.

Three regions can be observed:

- $\frac{\omega_i}{\omega_0} < 0.02$: the added damping is limited by the maximum allowed control gain g_{max}
- $0.02 < \frac{\omega_i}{\omega_0} < 0.2$: good amount of damping can be added for $g \approx 2$
- $0.2 < \frac{\omega_i}{\omega_0}$: the added damping becomes small due to the shape of the Root Locus (Figure 10)

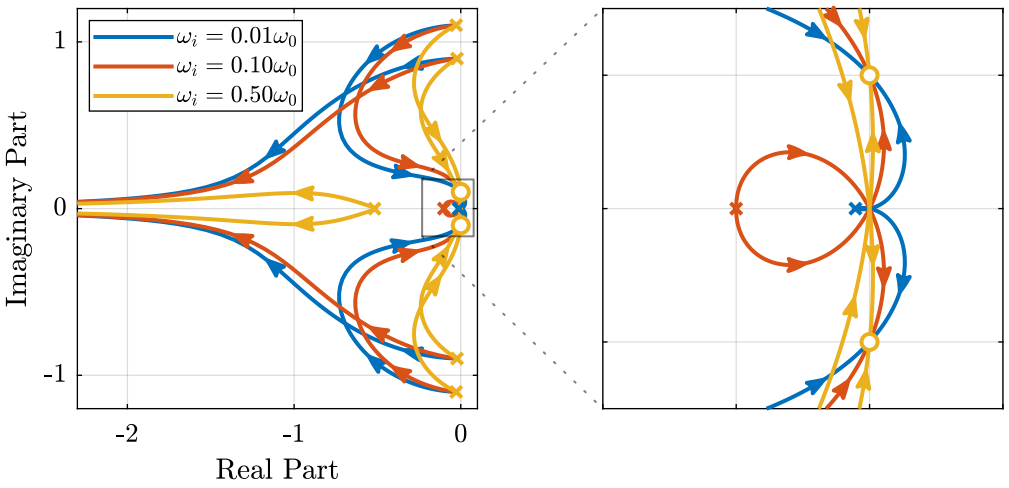

Figure 10: Root Locus for several HPF cut-off frequencies ω_i, $\Omega = 0.1\omega_0$

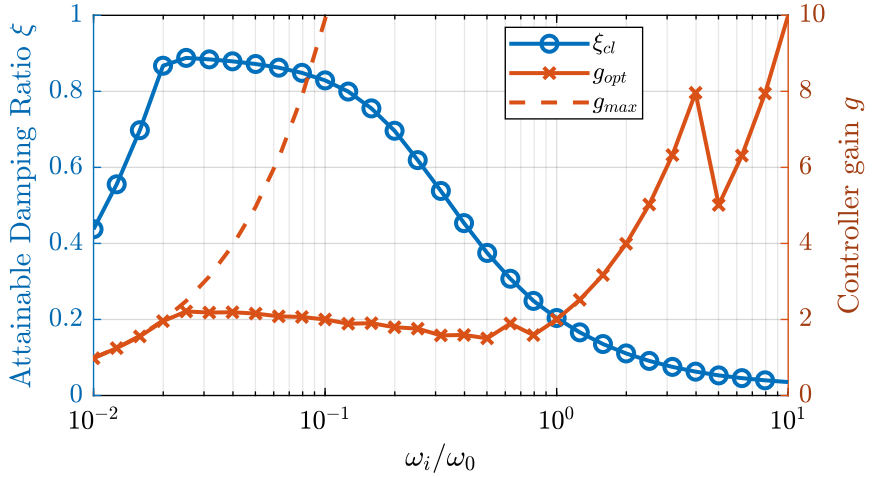

Figure 11: Attainable damping ratio ξ_{cl} as a function of the ratio ω_i/ω_0. Corresponding control gain g_{opt} and g_{max} are also shown

5 Integral Force Feedback with Parallel Springs

5.1 Stiffness in Parallel with the Force Sensor

As was explained in section 3.3, the instability when using decentralized IFF for rotating positioning platforms is due to Gyroscopic effects and more precisely to the negative stiffnesses induced by centrifugal forces. In this section additional springs in parallel with the force sensors are added to counteract this negative stiffness. Such springs are schematically shown in Figure 12 where k_a is the stiffness of the actuator and k_p the stiffness in parallel with the actuator and force sensor.

Amplified piezoelectric stack actuators can also be used for such purpose where a part of the piezoelectric stack is used as an actuator while the rest is used as a force sensor [5]. The parallel stiffness k_p then corresponds to the amplification structure. An example of such system is shown in Figure 13.

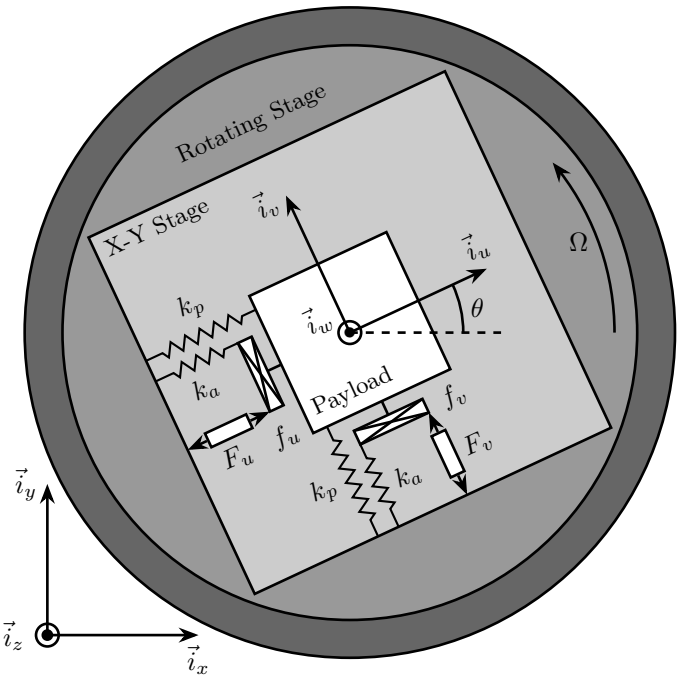

Figure 12: Studied system with additional springs in parallel with the actuators and force sensors

Figure 13: XY Piezoelectric Stage (XY25XS from Cedrat Technology)

5.2 Effect of the Parallel Stiffness on the Plant Dynamics

The forces measured by the sensors are equal to

$$\begin{bmatrix} f_u \\ f_v \end{bmatrix} = \begin{bmatrix} F_u \\ F_v \end{bmatrix} - (cs + k_a) \begin{bmatrix} d_u \\ d_v \end{bmatrix} \tag{19}$$

In order to keep the overall stiffness $k = k_a + k_p$ constant, a scalar parameter α ($0 \leq \alpha < 1$) is defined to describe the fraction of the total stiffness in parallel with the actuator and force sensor

$$k_p = \alpha k \tag{20a}$$
$$k_a = (1 - \alpha) k \tag{20b}$$

The equations of motion are derived and transformed in the Laplace domain

$$\begin{bmatrix} f_u \\ f_v \end{bmatrix} = \boldsymbol{G}_k \begin{bmatrix} F_u \\ F_v \end{bmatrix} \tag{21}$$

with $\boldsymbol{G}_k$ a 2×2 transfer function matrix

$$\boldsymbol{G}_k = \begin{bmatrix} \frac{\left(\frac{s^2}{{\omega_0}^2} - \frac{\Omega^2}{{\omega_0}^2} + \alpha\right)\left(\frac{s^2}{{\omega_0}^2} + 2\xi\frac{s}{\omega_0} + 1 - \frac{\Omega^2}{{\omega_0}^2}\right) + \left(2\frac{\Omega}{\omega_0}\frac{s}{\omega_0}\right)^2}{\left(\frac{s^2}{{\omega_0}^2} + 2\xi\frac{s}{\omega_0} + 1 - \frac{\Omega^2}{{\omega_0}^2}\right)^2 + \left(2\frac{\Omega}{\omega_0}\frac{s}{\omega_0}\right)^2} & \frac{-\left(2\xi\frac{s}{\omega_0} + 1 - \alpha\right)\left(2\frac{\Omega}{\omega_0}\frac{s}{\omega_0}\right)}{\left(\frac{s^2}{{\omega_0}^2} + 2\xi\frac{s}{\omega_0} + 1 - \frac{\Omega^2}{{\omega_0}^2}\right)^2 + \left(2\frac{\Omega}{\omega_0}\frac{s}{\omega_0}\right)^2} \\ \frac{\left(2\xi\frac{s}{\omega_0} + 1 - \alpha\right)\left(2\frac{\Omega}{\omega_0}\frac{s}{\omega_0}\right)}{\left(\frac{s^2}{{\omega_0}^2} + 2\xi\frac{s}{\omega_0} + 1 - \frac{\Omega^2}{{\omega_0}^2}\right)^2 + \left(2\frac{\Omega}{\omega_0}\frac{s}{\omega_0}\right)^2} & \frac{\left(\frac{s^2}{{\omega_0}^2} - \frac{\Omega^2}{{\omega_0}^2} + \alpha\right)\left(\frac{s^2}{{\omega_0}^2} + 2\xi\frac{s}{\omega_0} + 1 - \frac{\Omega^2}{{\omega_0}^2}\right) + \left(2\frac{\Omega}{\omega_0}\frac{s}{\omega_0}\right)^2}{\left(\frac{s^2}{{\omega_0}^2} + 2\xi\frac{s}{\omega_0} + 1 - \frac{\Omega^2}{{\omega_0}^2}\right)^2 + \left(2\frac{\Omega}{\omega_0}\frac{s}{\omega_0}\right)^2} \end{bmatrix} \tag{22}$$

Comparing $\boldsymbol{G}_k$ (22) with $\boldsymbol{G}_f$ (13) shows that while the poles of the system are kept the same, the zeros of the diagonal terms have changed. The two real zeros z_r (14b) that were inducing non-minimum phase behavior are transformed into complex conjugate zeros is Eq. 23 is verified.

$$\begin{aligned} \alpha &> \frac{\Omega^2}{{\omega_0}^2} \\ \Leftrightarrow k_p &> m\Omega^2 \end{aligned} \tag{23}$$

Thus, if the added parallel stiffness k_p is higher than the negative stiffness induced by centrifugal forces $m\Omega^2$, the direct dynamics from actuator to force sensor will show minimum phase behavior. This is confirmed by the Bode plot in Figure 14.

Figure 15 shows Root Loci plots for $k_p = 0$, $k_p < m\Omega^2$ and $k_p > m\Omega^2$ when K_F is a pure integrator (16). It is shown that if the added stiffness is higher than the maximum negative stiffness, the poles of the closed-loop system stay in the (stable) right half-plane, and hence the unconditional stability of IFF is recovered.

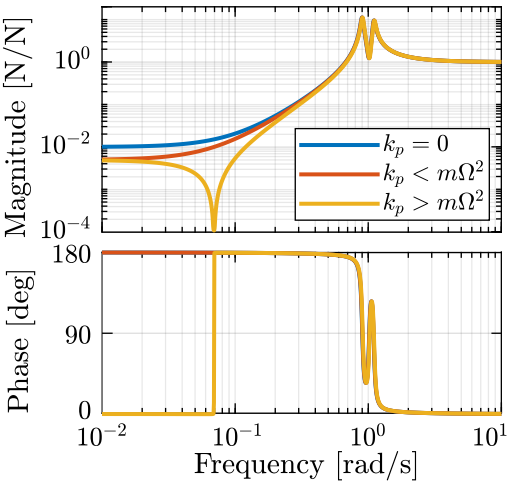

Figure 14: Bode Plot of f_u/F_u without parallel spring, with parallel springs with stiffness $k_p < m\Omega^2$ and $k_p > m\Omega^2$, $\Omega = 0.1\omega_0$

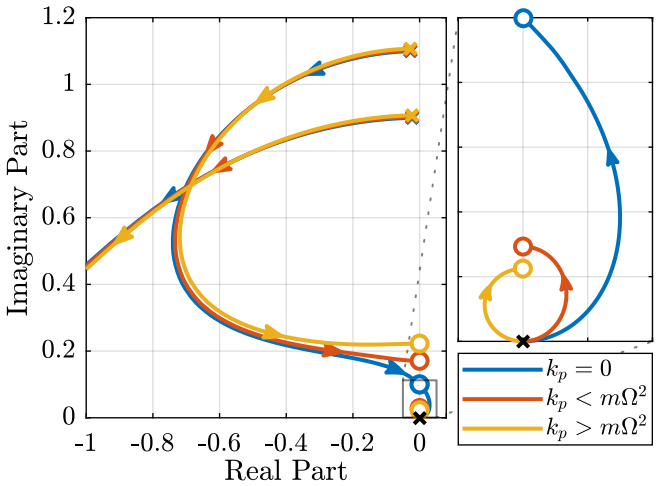

Figure 15: Root Locus for IFF without parallel spring, with parallel springs with stiffness $k_p < m\Omega^2$ and $k_p > m\Omega^2$, $\Omega = 0.1\omega_0$

5.3 Optimal Parallel Stiffness

Even though the parallel stiffness k_p has no impact on the open-loop poles (as the overall stiffness k stays constant), it has a large impact on the transmission zeros. Moreover, as the attainable damping is generally proportional to the distance between poles and zeros [6], the parallel stiffness k_p is foreseen to have a large impact on the attainable damping.

To study this effect, Root Locus plots for several parallel stiffnesses $k_p > m\Omega^2$ are shown in Figure 16a. The frequencies of the transmission zeros of the system are increasing with the parallel stiffness k_p and the associated attainable damping is reduced. Therefore the parallel stiffness k_p should not be taken too high while being larger than $m\Omega^2$ for stability reasons.

For any $k_p > m\Omega^2$, the control gain g can be tuned such that the maximum simultaneous damping ξ_{opt} is added to the resonances of the system. An example is shown in Figure 16b for $k_p = 5m\Omega^2$ where $\xi_{\text{opt}} \approx 0.83$ is obtained for a control gain $g_{\text{opt}} \approx 2\omega_0$.

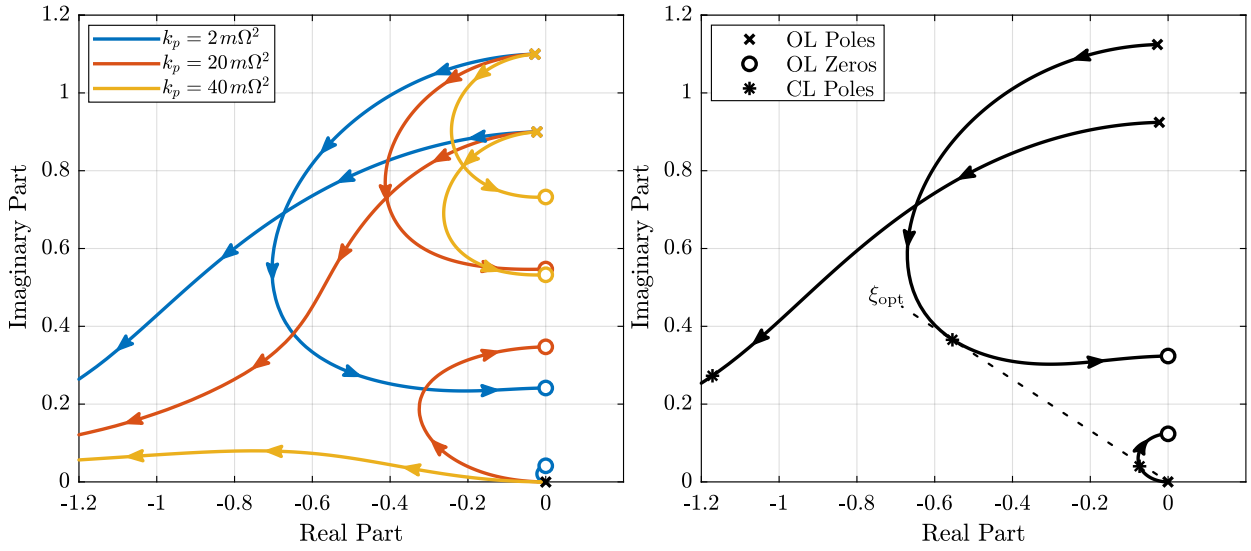

(a) Comparison of three parallel stiffnesses k_p

(b) $k_p = 5m\Omega^2$, optimal damping ξ_{opt} is shown

Figure 16: Root Locus for IFF when parallel stiffness k_p is added, $\Omega = 0.1\omega_0$

6 Comparison of the Proposed Modification to Decentralized Integral Force Feedback for Rotating Positioning Stages

Two modifications to the decentralized IFF for rotating positioning stages have been proposed.

The first modification concerns the controller and consists of adding an high pass filter to K_F (17). The system was shown to be stable for gains up to g_{max} (18).

The second proposed modification concerns the mechanical system. It was shown that if springs with a stiffness $k_p > m\Omega^2$ are added in parallel to the actuators and force sensors, decentralized IFF can be applied with unconditional stability.

These two methods are now compared in terms of added damping, closed-loop compliance and transmissibility. For the following comparisons, the cut-off frequency for the high pass filters is set to $\omega_i = 0.1\omega_0$ and the parallel springs have a stiffness $k_p = 5m\Omega^2$.

6.1 Comparison of the Attainable Damping

Figure 17 shows to Root Locus plots for the two proposed IFF techniques. While the two pairs of complex conjugate open-loop poles are identical for both techniques, the transmission zeros are not. This means that their closed-loop behavior will differ when large control gains are used.

It is interesting to note that the maximum added damping is very similar for both techniques and are reached for the same value of the gain in both cases $g_{\text{opt}} \approx 2\omega_0$.

6.2 Comparison Transmissibility and Compliance

The two proposed techniques are now compared in terms of closed-loop compliance and transmissibility.

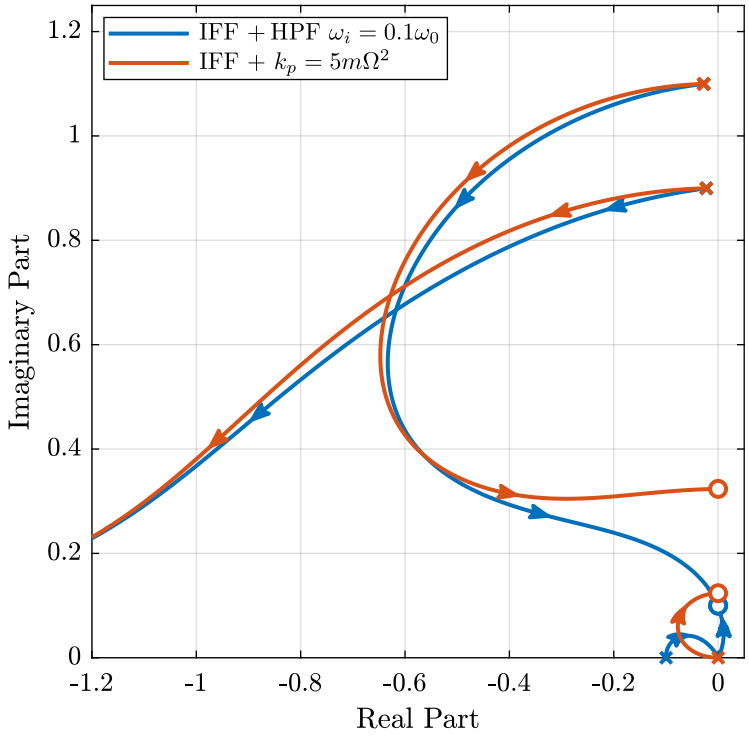

Figure 17: Root Locus for the two proposed modifications of decentralized IFF, $\Omega = 0.1\omega_0$

The compliance is defined as the transfer function from external forces applied to the payload to the displacement of the payload in an inertial frame. The transmissibility is the dynamics from the displacement of the rotating stage to the displacement of the payload. It is used to characterize how much vibration of the rotating stage is transmitted to the payload.

The two techniques are also compared with passive damping (Figure 1) where $c = c_{\text{crit}}$ is tuned to critically damp the resonance when the rotating speed is null

$$c_{\text{crit}} = 2\sqrt{km} \tag{24}$$

Very similar results are obtained for the two proposed decentralized IFF modifications in terms of compliance (Figure 18a) and transmissibility (Figure 18b). It is also confirmed that these two techniques can significantly damp the system's resonances.

Compared to passive damping, the two techniques degrades the compliance at low frequency (Figure 18a). They however do not degrades the transmissibility as high frequency as its the case with passive damping (Figure 18b).

7 Conclusion

Acknowledgment

This research benefited from a FRIA grant from the French Community of Belgium.

References

[1] T. Dehaeze, "Active damping of rotating positioning platforms," Source Code on Zonodo, 07 2020. [Online]. Available: https://doi.org/10.5281/zenodo.3894342

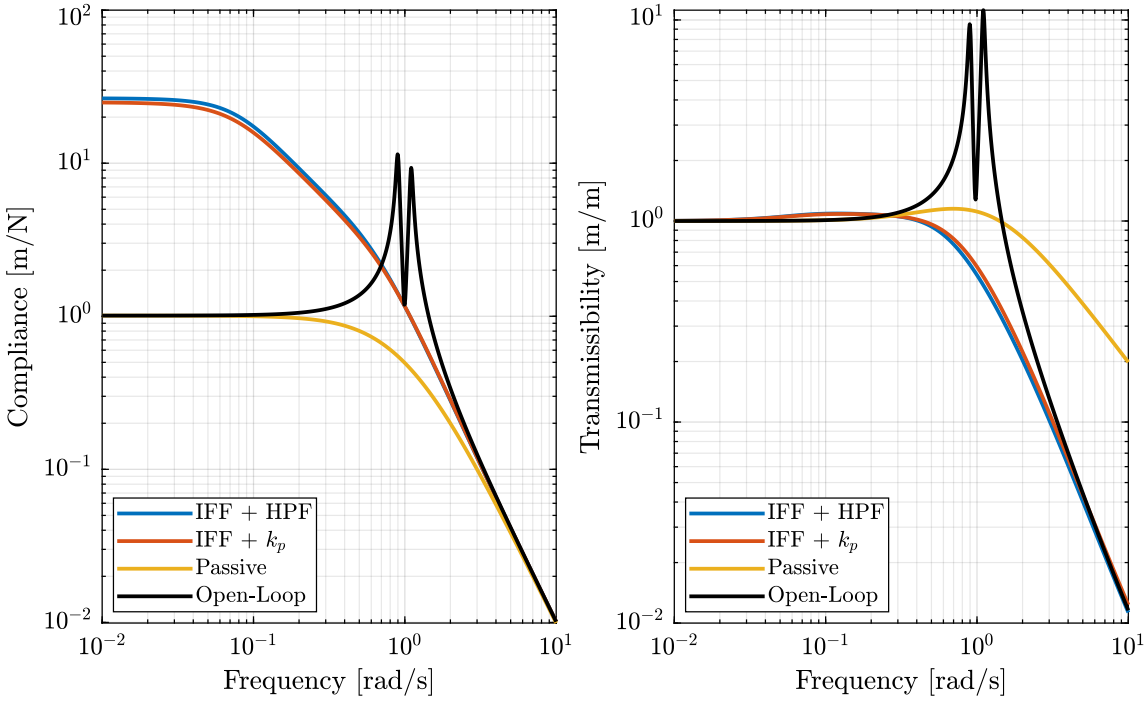

(a) Compliance (b) Transmissibility

Figure 18: Comparison of the two proposed Active Damping Techniques, $\Omega = 0.1\omega_0$

[2] A. Preumont, B. De Marneffe, and S. Krenk, "Transmission zeros in structural control with collocated multi-input/multi-output pairs," *Journal of guidance, control, and dynamics*, vol. 31, no. 2, pp. 428–432, 2008.

[3] S. Skogestad and I. Postlethwaite, *Multivariable Feedback Control: Analysis and Design*. John Wiley, 2007.

[4] A. Preumont, J.-P. Dufour, and C. Malekian, "Active damping by a local force feedback with piezoelectric actuators," in *32nd Structures, Structural Dynamics, and Materials Conference*. American Institute of Aeronautics and Astronautics, apr 1991. [Online]. Available: https://doi.org/10.2514/6.1991-989

[5] A. Souleille, T. Lampert, V. Lafarga, S. Hellegouarch, A. Rondineau, G. Rodrigues, and C. Collette, "A concept of active mount for space applications," *CEAS Space Journal*, vol. 10, no. 2, pp. 157–165, 2018.

[6] A. Preumont, *Vibration Control of Active Structures - Fourth Edition*, ser. Solid Mechanics and Its Applications. Springer International Publishing, 2018. [Online]. Available: https://doi.org/10.1007/978-3-319-72296-2